

Spherical Fraction Beamforming

Pierre Lecomte , Manuel Melon , and Laurent Simon , *Member, IEEE*

Abstract—This paper describes a beamforming method for one-eighth, quarter, and half-spaces, bounded by rigid planes. The proposed approach is based on the spherical fraction harmonic decomposition, similar to that of spherical harmonics decomposition for the whole sphere. The definition of these functions is given in detail. It is also proved that they form a sub-basis of the spherical harmonics, with a fraction-dependent normalization gain, which makes it easy to adapt from existing spherical harmonics implementation. Taking advantage of the rigid boundary condition, it is shown that the number of spherical fraction harmonics used to construct a beamformer is less than the number of spherical harmonics used in the case of an unbounded domain. However, image beams are generated and can degrade the performance of the beamformer. For the response to a plane wave, it is shown that the angular error on the maximum, as well as the directivity factor are a function of the spherical fraction under consideration, the plane wave direction of arrival and the degree of decomposition L . As the latter increases and the spherical fraction is large, these two parameters are converging towards the unbounded case values with fewer functions to evaluate. An application case is presented.

Index Terms—Beamforming, spherical harmonics.

I. INTRODUCTION

THE decomposition of an acoustic field on the basis of Spherical Harmonics (SH)s, relying on the Spherical Fourier Transform (SFT), is a widespread technique that serves as an entry point for the analysis of acoustic fields [1] for their reproduction [2] or for beamforming applications [3]. In the latter case, the principle consists in weighting the components of the SFT before summing them to obtain the beamformer output signal. The weights describe a beampattern. It is relatively straightforward to form rotationally invariant and axisymmetric beampatterns [4], when approaches such as delay-and-sum do not offer this characteristic [5]. By using a Spherical Microphone Array (SMA), it is then possible to analyze all directions homogeneously in the 4π steradian solid angle.

In many situations, however, not all these directions are relevant for sound field analysis. For example, as soon as the decomposition point is close to the limits of the acoustic domain

of interest, as in a room for example. In these situations, the sound sources all lie within the same angular sector from the SMA point of view. For example, a SMA placed on a table for teleconferencing applications has all its sources in the upper half space. Thus, the lower hemisphere is not relevant for the analysis and the reflections that occur there may even degrade the beamforming performance.

To overcome this difficulty, one solution is to consider only a part of the solid angle with a rigid condition at the boundaries of the domain [6], [7]. In order to operate the decomposition in this bounded space, a new basis of harmonics has to be calculated [8]–[10]. Another approach introduces a linear combination of SHs, orthonormal over the considered space, by using a Singular Value Decomposition (SVD) of the Gram matrix: the Spherical Slepian Functions [11], [12]. A comparative study between these two approaches is proposed in [13].

In this paper, a theoretical study is conducted for beamforming in the following domains: one-eighth, quarter and half-spaces. Each domain is bounded by rigid planes. Such configurations occur frequently in rooms: for instance, a corner of room consisting of the intersection of two vertical walls and the ceiling/floor is one-eighth of a space. Similarly, at the junctions between two walls, or a wall and the floor/ceiling, a quarter of space is described. Finally, the domain bounded by a single wall/ceiling/floor is an half-space. A possible application consists in placing a Spherical Fraction Microphone Array (SFMA) on one wall or at some wall junctions to carry a sound scene analysis through beamforming. Wide range of applications are then possible, ranging from medical supervision of the elderly, to intrusion detection, voice commands, etc.

More specifically, it is shown that the angular solution of the Helmholtz equation, i.e., the equivalent of the SFT on a Spherical Fraction (SF), is obtained by using a sub-basis of SHs, with a fraction-dependent normalization gain. These functions are called the Spherical Fraction Harmonics (SFH)s in this paper. As a consequence, the number of SFHs used to form a beampattern is less than the number of SHs, in the case of the unbounded domain. Then, it becomes possible to carry out an acoustic analysis using SFHs and SFMAs with minor modifications to existing SH implementations. However, the rigid boundary condition of the domain introduces image beampatterns whose main lobes can superimpose themselves on the main beampattern if the resolution of the decomposition is too low. The study of this compromise is carried out in this paper. Indeed, the number of functions to be manipulated represents the minimum number of microphones to be used, when designing a SFMA [8]. Thus, it is important to quantify the number of harmonics that can be spared on a SF configuration in comparison with the whole

Manuscript received June 12, 2020; revised September 28, 2020; accepted September 28, 2020. Date of publication October 29, 2020; date of current version November 19, 2020. This work was supported by Orange Labs. The Associate Editor coordinating the review of this manuscript and approving it for publication was Prof. Stefan Bilbao. (Corresponding author: Pierre Lecomte.)

Pierre Lecomte is with the Fluid Mechanics, and Acoustics Laboratory, LMFA, UMR CNRS 5509, Univ Lyon, Université Claude Bernard Lyon I, École Centrale de Lyon, INSA Lyon, 69134 Écully, France (e-mail: pierre.lecomte@univ-lyon1.fr).

Manuel Melon and Laurent Simon are with the Laboratoire d'Acoustique de l'Université du Mans (LAUM), UMR 6613, Institut d'Acoustique - Graduate School (IA-GS), CNRS, Le Mans Université, 72000 Le Mans, France (e-mail: manuel.melon@univ-lemans.fr; laurent.simon@univ-lemans.fr).

Digital Object Identifier 10.1109/TASLP.2020.3034516

spherical domain. The paper is organized as follows: in Section II the different definitions and mathematical notations used for the demonstrations are introduced. In particular, the different symmetries of SHs are demonstrated, using the Appendix A. From these symmetry relations and the Neumann boundary condition, the definition of SFHs is established in Section III and Appendix B. In particular, it is shown that SFHs form a basis of orthonormal functions in the SF (Appendix C). Similarly, it is shown that for the same degree of decomposition L , the number of these functions (Appendix D) decreases with the SF size in comparison with the whole sphere. Finally, it is demonstrated that the decomposition formulas of a sound pressure field in the SF are similar to those for the whole sphere. In Section IV, the beamforming output for a plane wave traveling in the SF is studied. The beampattern used is that of a directional Dirac, which then gives an analogy with the plane wave decomposition using SHs [14]. In comparison with the whole sphere, it is shown that image beampatterns appear symmetrically with respect to the domain boundaries. These images are superimposed and can degrade the performance of the beamformer in terms of the position of the maximum and of the Directivity Factor (DF). These two criteria are studied respectively in Secs. IV-B and IV-C. It is shown that the performance of the beamformer in the SF domains converges towards that of the whole sphere as the degree of truncation L increases and as the SF is large. Finally, in Section V, a case study is carried out for an acoustic field composed of two plane waves. The paper concludes in Section VI.

II. DEFINITIONS AND NOTATIONS

In this section, the definitions, notations and useful relations used throughout the paper are introduced.

A. Spherical Coordinate System

In the spherical coordinate system, a point at $\mathbf{r} = (r, \theta, \phi)$ is located by its radius r , with $r \in [0, \infty[$, its azimuth angle ϕ , with $\phi \in]0, 2\pi]$ and its zenith angle θ , with $\theta \in [0, \pi]$, such that:

$$\begin{cases} x = r \sin(\theta) \cos(\phi), \\ y = r \sin(\theta) \sin(\phi), \\ z = r \cos(\theta). \end{cases} \quad (1)$$

B. Spherical Fraction

a) Euclidian space division: In this paper, the three-dimensional Euclidian space and three possible divisions with planes $x = 0$, $y = 0$ and $z = 0$ are considered. One denotes such domains \mathbb{O}_q with $q \in \{1/8, 1/4, 1/2, 1\}$. Their definition is as follows:

$$\begin{cases} \mathbb{O}_{1/8} = \{(x, y, z) \in \mathbb{R}^3 | x \geq 0 \wedge y \geq 0 \wedge z \geq 0\}, \\ \mathbb{O}_{1/4} = \{(x, y, z) \in \mathbb{R}^3 | y \geq 0 \wedge z \geq 0\}, \\ \mathbb{O}_{1/2} = \{(x, y, z) \in \mathbb{R}^3 | z \geq 0\}, \\ \mathbb{O}_1 = \{(x, y, z) \in \mathbb{R}^3\}. \end{cases} \quad (2)$$

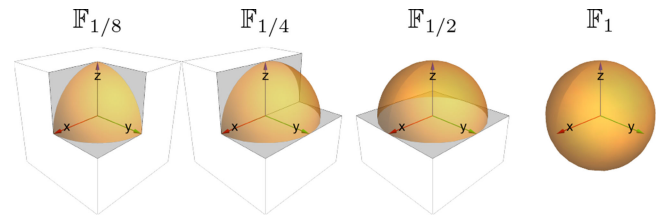


Fig. 1. Different Spherical Fraction domains \mathbb{F}_q under consideration. The \mathbb{O}_q plane boundaries are shown in gray.

In (2), (x, y, z) are the Cartesian coordinates, \wedge is the AND logical operator. The domains $\mathbb{O}_{1/8}$, $\mathbb{O}_{1/4}$, $\mathbb{O}_{1/2}$ and \mathbb{O}_1 , correspond to an eighth, a quarter, a half and the entire three-dimensional Euclidean space respectively. Note that the definition of \mathbb{O}_q for $q \in \{1/8, 1/4, 1/2\}$ is not unique. Indeed, when we divide the space \mathbb{O}_1 with the planes $x = 0$, $y = 0$ and $z = 0$ it is possible to construct 8 eighths of space, 12 quarter-spaces and 6 half-spaces. The demonstrations proposed in the rest of this work can be adapted to any of these configurations.

b) Spherical Fraction: From each domain \mathbb{O}_q , the Spherical Fractions (SF)s are defined by adding a condition on unit radial distance to the origin. The domains \mathbb{F}_q are given by:

$$\mathbb{F}_q = \mathbb{O}_q \cap \{x^2 + y^2 + z^2 = 1\}. \quad (3)$$

and are depicted in Fig. 1. Consequently, the SFs considered in this work correspond to an eighth, a quarter, a half sphere and the whole unit sphere.

C. Vector Space $\mathbb{L}^2(\mathbb{F}_q)$

A vector space of square-integrable functions for each SF domain \mathbb{F}_q is defined. This vector space is denoted $\mathbb{L}^2(\mathbb{F}_q)$.

a) Inner product. Let f and g be two functions defined in $\mathbb{L}^2(\mathbb{F}_q)$. The inner product in $\mathbb{L}^2(\mathbb{F}_q)$ is defined as [3]:

$$\langle f, g \rangle_{\mathbb{F}_q} = \int_{\mathbb{F}_q} f(\theta, \phi) g(\theta, \phi) \sin(\theta) d\theta d\phi. \quad (4)$$

b) Norm: In $\mathbb{L}^2(\mathbb{F}_q)$, the norm of a function f is given by:

$$\|f\|_{\mathbb{F}_q} = \sqrt{\langle f, f \rangle_{\mathbb{F}_q}}. \quad (5)$$

D. Spherical Harmonics

The homogeneous Helmholtz equation is given by:

$$\Delta p(\mathbf{r}, \omega) + k^2 p(\mathbf{r}, \omega) = 0, \quad (6)$$

where p is the acoustic pressure, k is the wave number. The Laplace operator is denoted Δ . Equation (6) is solved in the spherical coordinate system by using a separation of variables [15, p. 184] for the whole unit sphere (i.e., the domain \mathbb{F}_1 in (3)). The angular solutions form a basis on $\mathbb{L}^2(\mathbb{F}_1)$ called the SHs. The SHs are defined by:

$$Y_{l,m}(\theta, \phi) = \begin{cases} N_{l,|m|} P_l^m(\cos(\theta)) \cos(m\phi) & \text{for } m \geq 0 \\ N_{l,|m|} P_l^m(\cos(\theta)) \sin(m\phi) & \text{for } m < 0 \end{cases}, \quad (7)$$

where P_l^m are the associated Legendre polynomial of the first kind of degree l and order m , with $\{(l, m) \in (\mathbb{N}, \mathbb{Z}) \mid |m| \leq l\}$. $N_{l,|m|}$ is a normalization factor ensuring the orthonormality of the SHs on the unit sphere. It is given by:

$$N_{l,|m|} = \sqrt{\frac{(2 - \delta_m)(2l + 1)}{4\pi} \frac{(l - |m|)!}{(l + |m|)!}}, \quad (8)$$

where δ_m is the Kronecker delta function. In this paper, the real SHs definition is used, but the method is valid for complex SHs as well. The SHs form a basis on $\mathbb{L}^2(\mathbb{F}_1)$ and the following relationships are provided:

Orthonormality: For (l, m) and (l', m') pairs, one has:

$$\langle Y_{l,m}, Y_{l',m'} \rangle_{\mathbb{F}_1} = \delta_{l,l'} \delta_{m,m'}. \quad (9)$$

b) Spherical Fourier Transform: Let f be a function defined in $\mathbb{L}^2(\mathbb{F}_1)$. It can be decomposed on the SHs basis as:

$$f(\theta, \phi) = \sum_{l=0}^{\infty} \sum_{m=-l}^l f_{l,m} Y_{l,m}(\theta, \phi), \quad (10)$$

with the coefficients $f_{l,m}$ given by:

$$f_{l,m} = \langle f, Y_{l,m} \rangle_{\mathbb{F}_1}. \quad (11)$$

Equations (10) and (11) are the inverse and direct SFT respectively.

c) Parseval's relation: The Parseval's relation is given by [3]:

$$\langle f, f \rangle_{\mathbb{F}_1} = \sum_{l=0}^{\infty} \sum_{m=-l}^l f_{l,m}^2. \quad (12)$$

E. Symmetry Planes for the Spherical Harmonics

1) Azimuth Symmetry Planes: Equation (7) shows that the SHs have a periodicity $\frac{2\pi}{|m|}$ for $m \in \mathbb{Z}^*$ along the azimuth angle ϕ . According to the symmetries of the cosine and sine functions, the SHs have the azimuth even symmetry planes such that:

$$\begin{cases} \left\{ \phi = \frac{2n\pi}{m}, n \in \mathbb{Z} \right\} & \text{for } m > 0, \\ \left\{ \phi = \frac{2n\pi}{m} + \frac{\pi}{2m}, n \in \mathbb{Z} \right\} & \text{for } m < 0. \end{cases} \quad (13)$$

In the same way, they have the azimuth odd symmetry planes such that:

$$\begin{cases} \left\{ \phi = \frac{2n\pi}{m} + \frac{\pi}{2m}, n \in \mathbb{Z} \right\} & \text{for } m > 0, \\ \left\{ \phi = \frac{2n\pi}{m}, n \in \mathbb{Z} \right\} & \text{for } m < 0. \end{cases} \quad (14)$$

Note that for the case $l = m = 0$, the corresponding SH, $Y_{0,0} = 1$ has an infinite number of symmetry planes.

2) Zenith Symmetry Plane: The associated Legendre polynomials have the following parity relationship [16, 12.97]:

$$P_l^m(\cos(\theta)) = (-1)^{(l+m)} P_l^m(-\cos(\theta)), \quad (15)$$

which gives the zenith even symmetry plane such that:

$$\left\{ \theta = \frac{\pi}{2} \right\} \quad \text{for } (l + m) \in 2\mathbb{Z}. \quad (16)$$

TABLE I
CONDITIONS ON INDICES l AND m FOR THE CORRESPONDING SH TO PRESENT THE SYMMETRY PLANE DEFINED IN THE LEFT COLUMN

Plane	Conditions on (l, m)	
	Even symmetry	Odd symmetry
$x = 0$	$m \in 2\mathbb{N} \vee m \in 2\mathbb{Z}^- + 1$	$m \in 2\mathbb{N} + 1 \vee m \in 2\mathbb{Z}^-$
$y = 0$	$m \in \mathbb{N}$	$m \in \mathbb{Z}^-$
$z = 0$	$(l + m) \in 2\mathbb{Z}$	$(l + m) \in 2\mathbb{Z} + 1$

As well, the zenith odd symmetry plane is such that:

$$\left\{ \theta = \frac{\pi}{2} \right\} \quad \text{for } (l + m) \in 2\mathbb{Z} + 1. \quad (17)$$

3) $x = 0, y = 0, z = 0$ Symmetry Planes By using (1), the conditions $x = 0, y = 0$ and $z = 0$ are equivalent on the unit sphere to:

$$\begin{cases} x = 0 \Rightarrow \phi = \frac{\pi}{2} \vee \phi = \frac{3\pi}{2} \vee \theta = 0 \vee \theta = \pi \\ y = 0 \Rightarrow \phi = \pi \vee \phi = 2\pi \vee \theta = 0 \vee \theta = \pi \\ z = 0 \Rightarrow \theta = \frac{\pi}{2} \end{cases}, \quad (18)$$

where \vee stands for the logical OR. In order to find the SHs exhibiting symmetry planes $x = 0, y = 0$ or $z = 0$, one looks for the azimuth and zenith symmetry planes of (13), (14), (16) and (17) which respect the conditions of (18). By replacing θ and ϕ in (13), (14), (16) and (17) into (18), one obtains a set of indices l and m such that the corresponding SHs present the symmetry planes $x = 0, y = 0$ or $z = 0$. The demonstration is carried out in Appendix A. The results are summarized in Table I.

Note that the relationships in Table I for even symmetry were extrapolated in [17] from the SHs expression in Cartesian coordinate system at the first degrees. For the three planes $x = 0, y = 0$ and $z = 0$, if the sets of indices (l, m) for even and odd symmetries are joined together, one shows that $\{(l, m) \in (\mathbb{N}, \mathbb{Z}) \mid |m| \leq l\}$, which represents all possible SH indices. This means that for any SH $Y_{l,m}$, the planes $x = 0, y = 0$ and $z = 0$ are either odd or even symmetry planes.

III. SPHERICAL FRACTION HARMONICS

In this section, the SFHs are derived, which are the angular solutions of the Helmholtz equation in a SF \mathbb{F}_q bounded by Neumann conditions. It is shown that they form a basis of vector space $\mathbb{L}^2(\mathbb{F}_q)$. It should be noted that the SFHs established in this paper correspond to a particular case in a more general framework of establishing a complete basis of functions on portions of spheres bounded by rigid surfaces of fixed coordinates, studied in [10].

A. Rigid Boundary Condition and Symmetry Planes

From Euler equation, imposing a rigid boundary condition for the pressure means that the perpendicular particle velocity vanishes. This results in Neumann condition on the boundaries. One considers the angular part of the Helmholtz equation solution, i.e., the SHs of (7): in order to respect the rigid boundary

TABLE II
SET \mathbb{M}_q DEFINITION. NUMBER $Q_q(L)$ UP TO DEGREE L SFHS NORM N_q . $[\cdot]$ IS THE FLOOR FUNCTION

SF \mathbb{F}_q	\mathbb{M}_q definition	SFHs number $Q_q(L)$ up to maximum degree L	SFHs Norm N_q .
$\mathbb{F}_{1/8}$	$\{(l, m) \in (\mathbb{N}, \mathbb{Z}) \mid m \leq l \wedge l \in 2\mathbb{N} \wedge m \in 2\mathbb{N}\}$	$\frac{1}{2} \left(\left\lfloor \frac{L}{2} \right\rfloor + 1 \right) \left(\left\lfloor \frac{L}{2} \right\rfloor + 2 \right)$	$2\sqrt{2}$
$\mathbb{F}_{1/4}$	$\{(l, m) \in (\mathbb{N}, \mathbb{Z}) \mid m \leq l \wedge m \in \mathbb{N} \wedge (l+m) \in 2\mathbb{N}\}$	$\frac{1}{2} \left[\left(\left\lfloor \frac{L}{2} \right\rfloor + 1 \right) \left(\left\lfloor \frac{L}{2} \right\rfloor + 2 \right) + \left(\left\lfloor \frac{L-1}{2} \right\rfloor + 1 \right) \left(\left\lfloor \frac{L-1}{2} \right\rfloor + 2 \right) \right]$	2
$\mathbb{F}_{1/2}$	$\{(l, m) \in (\mathbb{N}, \mathbb{Z}) \mid m \leq l \wedge (l+m) \in 2\mathbb{Z}\}$	$\frac{1}{2}(L+1)(L+2)$	$\sqrt{2}$
\mathbb{F}_1	$\{(l, m) \in (\mathbb{N}, \mathbb{Z}) \mid m \leq l\}$	$(L+1)^2$	1

condition, one should have a zero-valued pressure derivative with respect to θ and ϕ respectively. Moreover, from (7), the SHs are C^∞ class functions, as the product of polynomials and trigonometric functions. Besides, they exhibit several even symmetry planes as shown in Section II-E. Thus, on these planes, their normal derivative is necessarily zero. Therefore, for the SHs, looking for a zero-valued normal derivative is equivalent to looking for particular even symmetry planes.

B. Spherical Fraction Harmonics

For each SF \mathbb{F}_q , a SHs family is extracted from the SHs basis by only keeping those that have a null derivative with respect to θ and ϕ on the \mathbb{F}_q domain boundaries. Such harmonics are called SFHs and denoted $Y_{l,m,q}$. They are defined on $\mathbb{L}^2(\mathbb{F}_1)$ by:

$$Y_{l,m,q}(\theta, \phi) = N_q Y_{l,m}(\theta, \phi) \quad \text{for } (l, m) \in \mathbb{M}_q. \quad (19)$$

In (19), N_q represents the SFH norm which is derived in Appendix C, and \mathbb{M}_q are sets defined in the next section.

C. Sets \mathbb{M}_q

As shown in Section III-A, finding the harmonics $Y_{l,m,q}$ that fit with the rigid boundary condition is equivalent to finding the SHs that have even symmetry planes containing the \mathbb{F}_q domain boundaries. The \mathbb{F}_q domain definition is recalled from (3). Then, using the corresponding conditions on (l, m) indices in Table I, a set of (l, m) indices is build and denoted \mathbb{M}_q . This set gives the SH indices (l, m) to construct the SFH family $Y_{l,m,q}$. The derivation of the sets \mathbb{M}_q is given in Appendix B for $q \in \{1/8, 1/4, 1/2\}$. The results are summarized in Table II.

D. SFHs Orthonormality

As the SFHs family $Y_{l,m,q}$ is a subset of the SH family, they are orthogonal on $\mathbb{L}^2(\mathbb{F}_1)$. To prove that they are orthonormal on $\mathbb{L}^2(\mathbb{F}_q)$, their symmetry properties are used. An example of demonstration is carried out in Appendix C. As the family $Y_{l,m,q}$ is orthogonal, it is a linear independent family in $\mathbb{L}^2(\mathbb{F}_q)$ and one has:

$$\langle Y_{l,m,q}, Y_{l',m',q} \rangle_{\mathbb{F}_q} = \delta_{l,l'} \delta_{m,m'}. \quad (20)$$

Note that orthonormality is ensured by norm N_q in (19), whose values are given in Table II.

E. SFHs Completeness

The last step to prove that the SFs family $Y_{l,m,q}$ forms a complete basis of $\mathbb{L}^2(\mathbb{F}_q)$ is to show their spanning property over $\mathbb{L}^2(\mathbb{F}_q)$. This proof of completeness can be done using

the Sturm-Liouville theory [18, p. 79]. In [10], it is described how this theory is applied for the case of harmonic functions on spherical portions with Neumann or Dirichlet boundary conditions. Consequently, any function f defined on $\mathbb{L}^2(\mathbb{F}_q)$, can be represented as a linear combination $f_{l,m} Y_{l,m,q}$ such that:

$$f(\theta, \phi) = \sum_{l=0}^{\infty} \sum_{\substack{m=-l \\ (l,m) \in \mathbb{M}_q}}^l f_{l,m} Y_{l,m,q}(\theta, \phi), \quad (21)$$

where $f_{l,m}$ are the combination weights. To find the latter, let multiply both sides of (21) by $Y_{l',m',q}$, integrate the result over \mathbb{F}_q and use (20) to show that:

$$f_{l,m} = \langle f, Y_{l,m,q} \rangle_{\mathbb{F}_q}. \quad (22)$$

Equations (21) and (22) are the inverse and direct SF Fourier Transforms (SFFT) respectively. Finally, the family $Y_{l,m,q}$ is orthonormal and spans the vector space $\mathbb{L}^2(\mathbb{F}_q)$, thus it is a complete basis of $\mathbb{L}^2(\mathbb{F}_q)$. In particular, the Parseval relation of (12) is valid.

F. SFHs Number up to a Degree L

Up to L , the SFHs number $Q_q(L)$ for each SF \mathbb{F}_q is given by:

$$Q_q(L) = \sum_{l=0}^L \sum_{\substack{m=-l \\ (l,m) \in \mathbb{M}_q}}^l 1. \quad (23)$$

Closed-form expressions are given in Tab II. Their derivation is done in Appendix D. The number $Q_p(L)$ is plotted from $L = 0$ to $L = 30$ in Fig. 2. From Fig. 2(a), one observes that $Q_q(L) \leq Q_1(L)$. That is to say, the SFHs number $Q_q(L)$, for the bounded domains \mathbb{F}_q is less than the number of SHs for the unbounded domain \mathbb{F}_1 . In addition, as shown in Fig. 2(b), the ratio $Q_q(L)/Q_1(L)$ decreases with increasing L and converges to the SF number q . For instance, the domain $\mathbb{F}_{1/8}$ represents one eighth of the domain \mathbb{F}_1 , i.e., the unit sphere. Thus, the number $Q_{1/8}/Q_1$ converges to $1/8$ when L , increases. Similarly, the numbers $Q_{1/4}/Q_1, Q_{1/2}/Q_1$ converge to $1/4$ and $1/2$ respectively.

Thus, by bounding the spherical domain, one can significantly reduce the number of harmonics to decompose the sound pressure field. This is of great interest as the SFHs number represents the minimum number of microphones in a SFMA for an accurate decomposition [8].

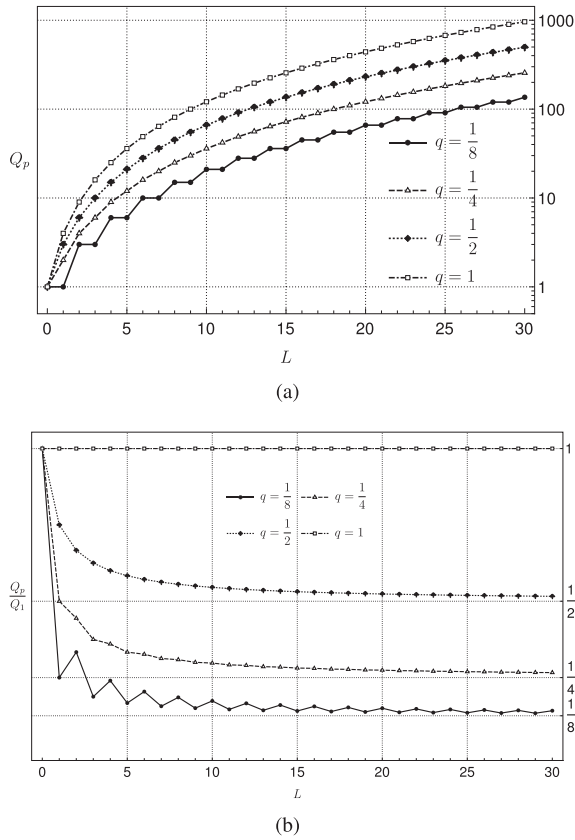


Fig. 2. (a) Q_q : SFHs number up to degree L . (b) Ratio Q_q/Q_1 versus maximum degree L .

G. Sound Pressure Field Representation With SFHs

Let us consider a domain \mathbb{O}_q from (2). Following the same method as for the free field case [15], the solutions of the homogeneous Helmholtz equation (6) are:

$$p(k, r, \theta, \phi) = \sum_{l=0}^{\infty} \sum_{\substack{m=-l \\ (l,m) \in \mathbb{M}_q}}^l i^l j_l(kr) b_{l,m,p} Y_{l,m,q}(\theta, \phi). \quad (24)$$

In (24), $i = \sqrt{-1}$, and j_l are the spherical Bessel functions of degree l . The coefficients $b_{l,m}$ are given from the pressure SFHs coefficients $p_{l,m}$ using (22) and the orthonormality of SFHs (20):

$$p_{l,m,p} = i^l j_l(kr) b_{l,m,p}. \quad (25)$$

Plane wave representation. Similarly to the free field case [19], a unit-amplitude plane wave in the rigid bounded domain \mathbb{G}_q , with the Direction Of Arrival (DOA) (θ_s, ϕ_s) , is represented as follows:

$$p(k, r, \theta, \phi) = \sum_{l=0}^{\infty} \sum_{\substack{m=-l \\ (l,m) \in \mathbb{M}_q}}^l i^l j_l(kr) Y_{l,m,q}(\theta_s, \phi_s) Y_{l,m,q}(\theta, \phi), \quad (26)$$

which gives, by identification with (24) the following pressure SFFT coefficients:

$$b_{l,m,p} = Y_{l,m,q}(\theta_s, \phi_s). \quad (27)$$

To prove (26), the image source approach [20] is used. In the rigid-bounded domain \mathbb{O}_q , the acoustic pressure due to a source is equivalent to the sum of the acoustic pressure of the source in the unbounded domain plus the acoustic pressure of the image sources which are placed symmetrically with respect to the rigid boundaries. An example of demonstration is carried out for the rigid-bounded domain $\mathbb{O}_{1/2}$ in Appendix E.

IV. SF BEAMFORMING

In this section, SFH beamforming on the different SF \mathbb{F}_q is studied. The SF beamforming is a modal beamforming [4]. Therefore, the beamformer output $y(\theta, \phi)$ is a weighted sum of coefficients $b_{l,m}$ in (25):

$$y_q(\theta, \phi) = \sum_{l=0}^{\infty} \sum_{\substack{m=-l \\ (l,m) \in \mathbb{M}_q}}^l w_{l,m,p} b_{l,m,p}. \quad (28)$$

In (28), $w_{l,m,p}$ are the SFH weights for a beampattern $w(\theta, \phi)$.

A. Beamformer Output for a Unit-Amplitude Plane Wave

A directional Dirac is chosen as weighting function, with the steering angle (θ_s, ϕ_s) , such that:

$$w(\theta, \phi) = \delta(\theta_s - \theta) \delta(\phi_s - \phi). \quad (29)$$

From (22), it follows:

$$w_{l,m,p} = Y_{l,m,q}(\theta, \phi). \quad (30)$$

Finally, from plane wave coefficients, (27) and weights of (30) applied to (28), the following beamformer output express as:

$$y_q(\theta, \phi) = \sum_{l=0}^{\infty} \sum_{\substack{m=-l \\ (l,m) \in \mathbb{M}_q}}^l Y_{l,m,q}(\theta, \phi) Y_{l,m,q}(\theta_s, \phi_s). \quad (31)$$

This latter equation corresponds to the Inverse SFFT of (21) for a plane wave with DOA (θ_s, ϕ_s) . It is also referred to as the plane wave decomposition for \mathbb{F}_1 domain [14]. (31) can be further simplified with Legendre Polynomial in the case of \mathbb{F}_1 , by using the addition theorem of SHs [16]:

$$y_1(\Theta) = \sum_{l=0}^{\infty} \frac{2l+1}{4\pi} P_l(\cos(\Theta)), \quad (32)$$

where P_l represents the Legendre polynomial of degree l . The angle Θ is the angle between directions (θ, ϕ) and (θ_s, ϕ_s) . It is given by:

$$\cos(\Theta) = \sin(\theta) \sin(\theta_s) \cos(\phi - \phi_s) + \cos(\theta) \cos(\theta_s). \quad (33)$$

In practice, (31) is truncated to a maximum degree L . This truncation determines the beampattern main lobe width and side lobe heights [14]. The normalized magnitude $|y_q(\theta, \phi)/y_q(\theta_s, \phi_s)|$ is plotted for $(\theta, \phi) \in \mathbb{F}_1$ for two maximum degrees $L = 4$ and $L = 6$ and for two plane waves with DOA $(\theta_s = 45^\circ, \phi_s = 45^\circ)$

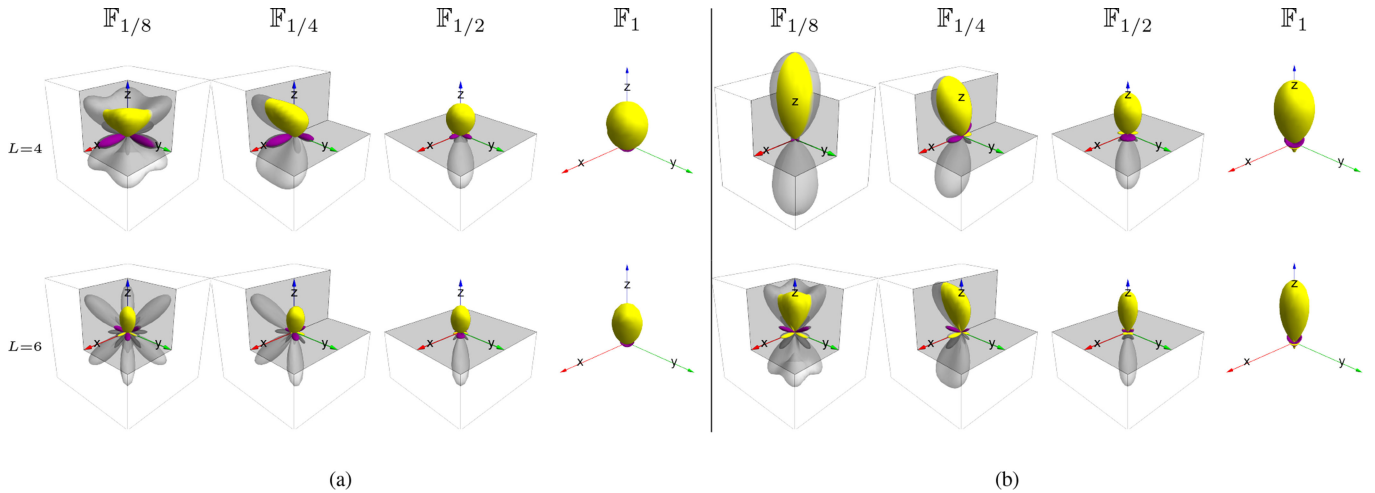


Fig. 3. Normalized magnitude $|y_q(\theta, \phi)/y_q(\phi_s, \phi_s)|$ for the different SF \mathbb{F}_q , for a plane wave with DOA (a) $(\theta_s = 45^\circ, \phi_s = 45^\circ)$ and (b) $(\theta_s = 27^\circ, \phi_s = 45^\circ)$. First row $L = 4$, second row $L = 6$. The gray planes show the domain \mathbb{Q}_q boundaries. For each index q , the function is plotted in gray when outside the corresponding domain \mathbb{F}_q . The dark/purple regions are of negative sign and the bright/yellow region are of positive sign.

and $(\theta_s = 27^\circ, \phi_s = 45^\circ)$ in Fig. 3. For sake of comparison, the plane wave DOAs (θ_s, ϕ_s) are chosen in $\mathbb{F}_{1/4}$, such as it is contained in all the SF \mathbb{F}_q .

a) Observations: The rigid boundaries impact on the beam pattern shapes and performance in terms of directivity and position of the maximum, in comparison with the free field case given at the right column of Fig 3. As q increases, or equivalently as the SF \mathbb{F}_q is less bounded, the beam pattern shape tends towards that of \mathbb{F}_1 . In the same way, one can notice that increasing L decreases the influence of the rigid boundaries on the shape of the beam pattern, which tends more rapidly towards the one of the free field case in \mathbb{F}_1 . Finally, by comparing Figs. 3(a) and 3(b), one notices that the plane wave DOA (θ_s, ϕ_s) influences the beam pattern shape for SF $\mathbb{F}_{1/8}, \mathbb{F}_{1/4}, \mathbb{F}_{1/2}$. For the free field case (\mathbb{F}_1), the shape of the beam pattern is invariant to the plane wave DOA [4].

b) Interpretation: Following the image source approach, the beam patterns obtained in SF \mathbb{F}_q can be considered as the superposition of free field beam patterns in (32) for plane waves whose DOAs are symmetric with respect to the domain boundaries [6]. Depending on the plane wave DOA, the superposition and interference with the image beam patterns influence the resulting shape in \mathbb{F}_q and break the rotational-invariance property that one has in the free field case [4]. This influence depends on the plane wave DOA with respect to the \mathbb{F}_q domain boundaries and to the beam pattern main lobe width and side lobes amplitudes. For a beam pattern in free field, the main lobe width decreases as well as the side lobes amplitudes when the degree L increases [14]. Thus, as the degree L increases, the interferences with the image beam patterns outside \mathbb{F}_q decrease, which can be observed by comparing rows $L = 4$ and $L = 6$ in Fig. 3. However, it is important to remember that, to build beam patterns in the domain \mathbb{F}_q , the more bounded the SF \mathbb{F}_q is, the less SFHs are needed to build a beam pattern as shown in Fig. 2. In the following sections, one details the beam pattern performance as a function of the SF \mathbb{F}_q , the degree L and the plane wave DOA (θ_s, ϕ_s) .

B. Angular Error

A first criterion to assess the quality of the proposed method is the angular error between the beam pattern maximum and the plane wave DOA (θ_s, ϕ_s) . As the beam pattern used is a directional Dirac (29), in the free field case, its maximum corresponds to the plane wave DOA (θ_s, ϕ_s) . However, for the other SFs \mathbb{F}_q with $q \in \{1/8, 1/4, 1/2\}$, the image beam patterns may interfere constructively, which tends to deflect the resulting beam pattern maximum. The direction of this maximum is denoted by (θ_q, ϕ_q) . The angular error, denoted Ψ_q , is derived from (33) as:

$$\Psi_q = \arccos(\sin(\theta_q) \sin(\theta_s) \cos(\phi_q - \phi_s) + \cos(\theta_q) \cos(\theta_s)). \quad (34)$$

The angular error Ψ_q is plotted for $L \in \{4, 8, 30\}$, and for $q \in \{1/8, 1/4, 1/2\}$ in Fig. 4. Note that $\Psi_{1/4}$ is symmetrical with respect to the plane $\phi_s = 90^\circ$ and $\Psi_{1/2}$ does not depend on the angle ϕ_s . Therefore, for all SF, Ψ is plotted for $(\theta_s, \phi_s) \in (0, 90^\circ) \times (0, 90^\circ)$. From Fig. 4, it can be observed that the angular error Ψ_q increases as one moves away from the domain boundaries. This increase reaches a maximum and then Ψ_q falls abruptly down to a zone of very low error. The latter widens as L increases. Likewise, the maximum error Ψ_q decreases and its position moves closer to the limits of the domain as L increases. The increase of Ψ_q as the plane wave DOA (θ_s, ϕ_s) moves away from the domain boundary shows that the main lobe superposition from image beam patterns tends to keep the maximum of the resulting beam pattern on the domain boundary. This can be seen on the example of Fig. 3(b) for $L = 4$ and $q = 1/8$ or $q = 1/4$.

To better analyze this, let us consider the case where only one image beam pattern is present, as for $q = 1/2$. Then, the resulting beam pattern is the superposition of two free field beam patterns of (32) for two plane waves whose DOAs are separated by an angle Θ , as given in (33), and symmetrically distributed

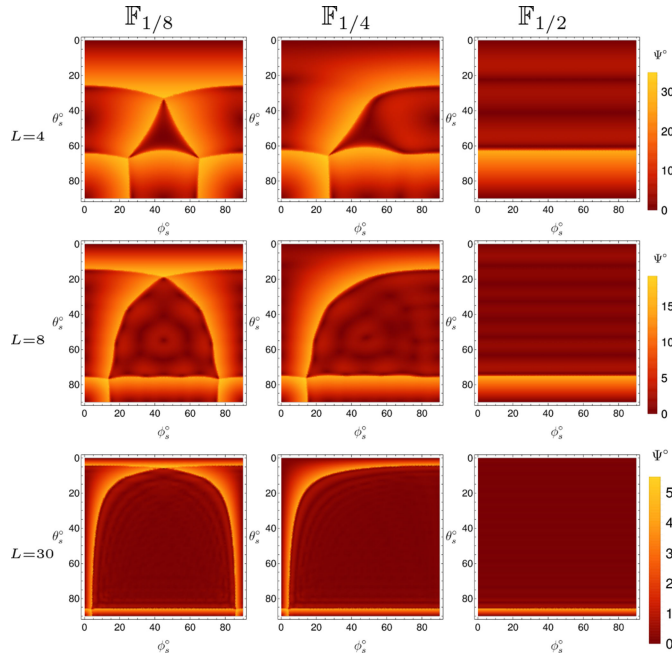


Fig. 4. Angular error Ψ between the beampattern maximum (θ_q, ϕ_q) and the plane wave DOA (θ_s, ϕ_s) , for all possible DOAs $(\theta_s, \phi_s) \in (0, 90^\circ) \times (0, 90^\circ)$ for the SF \mathbb{F}_q with $q \in \{1/8, 1/4, 1/2\}$ and for $L \in \{4, 8, 30\}$.

around $\theta = 90^\circ$. Therefore, the angle $\Theta/2$ is the angular distance between the rigid boundary and the main beampattern. In Fig. 5, the two free field beampatterns are represented as a function of angle θ for $L = 8$, $\Theta = 20^\circ$ (Fig. 5(a)) and $\Theta = 40^\circ$ (Fig. 5(b)) by the dotted and dashed curves respectively. The symmetry plane corresponding to $\theta = 90^\circ$ is represented by the thick line. The resulting beampattern is the sum of these two functions and is shown as a solid line. From Fig. 5, it can be seen that resulting beampattern present a single global maximum, located at $\theta = 90^\circ$, when:

$$\Theta \leq \Theta_{\text{lim}}, \quad (35)$$

where Θ_{lim} is the Full Width at Half the Maximum (FWHM) of the free field beampattern of (32). Beyond this angular distance, the resulting beampattern has two maxima located symmetrically with respect to the rigid boundary (Fig. 5(b)). The quantity Θ_{lim} is plotted versus the degree L in Fig. 6. For instance, at $L = 8$ one has $\Theta_{\text{lim}} \simeq 28.33^\circ$, for the SF $\mathbb{F}_{1/2}$, this results in a limit zenith angle $\theta_{s,\text{lim}} = 90^\circ - \Theta_{\text{lim}}/2 \simeq 75.83^\circ$ (see Fig. 4). For this angle, the maximum is still at $\theta = 90^\circ$ and the angular error $\Phi_{1/2}$ reaches its maximum as observed in Fig. 4. When $\Theta \geq \Theta_{\text{lim}}$ the influence of the image beampattern main lobes decreases and beyond the first zeros of the free field beampattern, the angular error Ψ_q is governed by the image beampattern side lobes superposition. This behaviour is similar for the SFs with $q \in \{1/8, 1/4\}$ even if more image beampatterns are superimposed in these cases. More specifically, this analysis is intimately linked to the resolution given by the plane wave decomposition with SHs [14]. In the free field case, if more than one plane wave is present, the resolution that allows to discriminate the directions of two plane waves is given by $\Theta_{\text{lim}} \simeq \frac{\pi}{L}$, when using

the Rayleigh criterion [3]. The situation is similar here when the SF is rigid-bounded: this introduces several image plane waves which can compromise the analysis when the angles between the plane waves are less than the resolution at degree L .

a) *Mean value:* By averaging the angular error Ψ_q of (34) for all possible DOAs in the solid angle offered by the SF \mathbb{F}_q , one obtains the mean value, denoted $\bar{\Psi}_q$ and given by:

$$\bar{\Psi}_q = \frac{1}{q4\pi} \int_{\mathbb{F}_q} \Psi_q(\theta_s, \phi_s) \sin(\theta_s) d\theta_s d\phi_s. \quad (36)$$

This quantity is plotted versus maximum degree L in Fig. 7, where it can be observed that the average angular error decreases rapidly as the degree increases. Indeed, as discussed in Section IV-B, when L increases, the main lobe width decreases as well as the amplitude of the side lobes. As a result, the influence of the image beampatterns decreases and the mean angular error on the maximum is smaller. This criterion is useful when designing a SF regular beamformer. It must be set against the number $Q_q(L)$ of SFHs involved. For instance, the angular error falls below 1° from $L = 24$ for $\mathbb{F}_{1/8}$, $L = 20$ for $\mathbb{F}_{1/4}$ of sphere and $L = 15$ for $\mathbb{F}_{1/2}$ for a gain of about 6.87, 3.64, 1.88 times fewer SFHs than SHs respectively.

C. Directivity Factor

A second criterion for estimating the performance of the proposed method is the Directivity Factor (DF). It is given by the following formula [3]:

$$\text{DF}_q(\theta_s, \phi_s) = \frac{|y_q(\theta_s, \phi_s)|^2}{\frac{1}{4\pi} \int_{\mathbb{F}_q} |y_q(\theta, \phi)|^2 \sin(\theta) d\theta d\phi}, \quad (37)$$

where y_q is defined in (31). Equation (37) can be interpreted as the Signal-to-Noise Ratio (SNR) of an output signal when the observation direction corresponds to the plane-wave DOA and a spherically isotropic noise sound field. When working in the bounded domains, i.e., for $q \in \{1/8, 1/4, 1/2\}$, the noise field is evaluated for a SF, and not on the whole sphere. Therefore, the denominator of (37) reduces which results in an improved DF [21]. For instance, for $L = 0$, the beampattern shape is omnidirectional and identical for all SFs \mathbb{F}_q . However, one has $\text{DF}_{1/8} = 8$ and $\text{DF}_1 = 1$, as the isotropic noise field is evaluated on a spherical region 8 times smaller for $q = 1/8$ in comparison with $q = 1$. By replacing $y_q(\theta, \phi)$ in numerator of (37) from (31), and by using Parseval relation of (12) for the denominator, it can be shown that:

$$\text{DF}_q(\theta_s, \phi_s) = 4\pi \sum_{l=0}^{\infty} \sum_{\substack{m=-l \\ (l,m) \in \mathbb{M}_q}}^l Y_{l,m,q}(\theta_s, \phi_s)^2. \quad (38)$$

In the case of \mathbb{F}_1 , up to a maximum degree L , one has:

$$\text{DF}_1 = Q_1(L) = (L+1)^2. \quad (39)$$

Equation (39) is obtained by using the addition theorem of SHs [16]. Therefore, in the case of the whole spherical domain \mathbb{F}_1 , the DF is independent of the steering angle. However, for the other SFs \mathbb{F}_q with $q \in \{1/8, 1/4, 1/2\}$, (38) can not be simplified. To study the dependence of DF with the plane wave

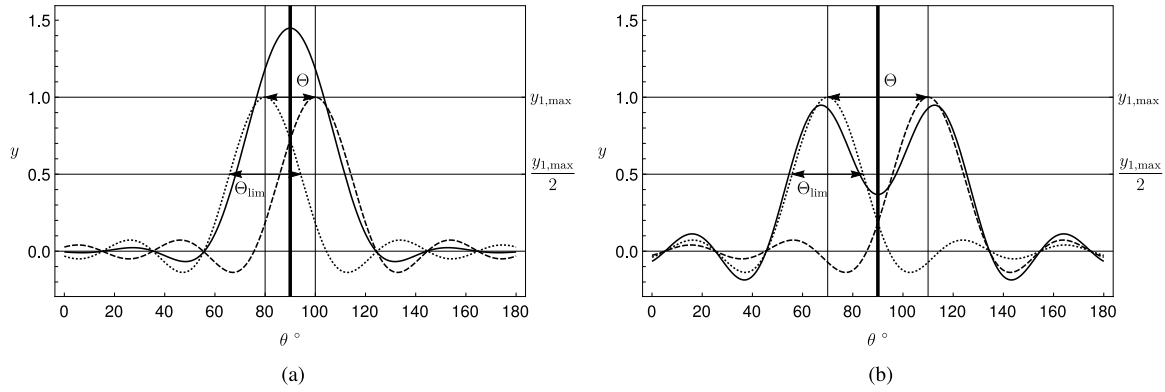


Fig. 5. Free field beampatterns at $L = 8$ in dashed and dotted lines, for plane waves whose DOAs are symmetrically distributed around $\theta = 90^\circ$ (thick line). The angular distance is: (a) $\Theta = 20^\circ$, (b) $\Theta = 40^\circ$. The sum of these two functions is shown in solid line. The FWHM angular distance is denoted Θ_{lim} and is shown on a free field beampattern. .

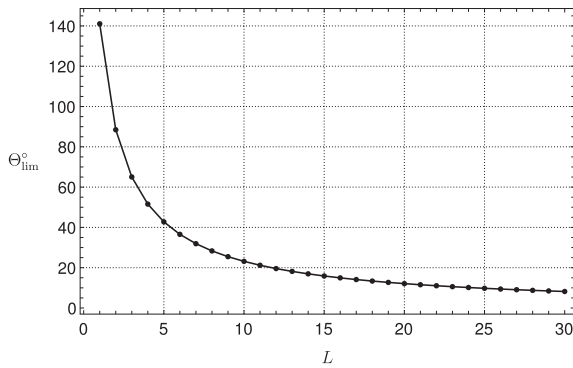


Fig. 6. FWHM angular distance as a function of maximum degree L for a free field beampattern.

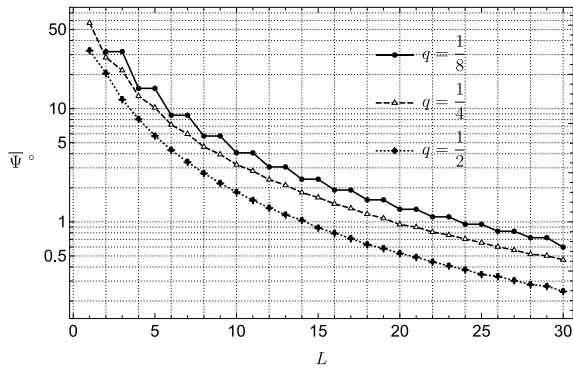


Fig. 7. Average angular error $\bar{\Psi}_q$ in degrees.

DOA, the Directivity Index (DI), defined in (40), is plotted in Fig. 8 for $L \in \{4, 8, 30\}$ with

$$\text{DI}_q = 10 \log(\text{DF}_q). \quad (40)$$

In Fig. 8 the DI is constant over a larger area as the SF \mathbb{F}_p is larger and as L increases. As for the angular error analysis in Section IV-B, this means that the interferences of the image lobes are less and less significant and that the beampattern y_q tends

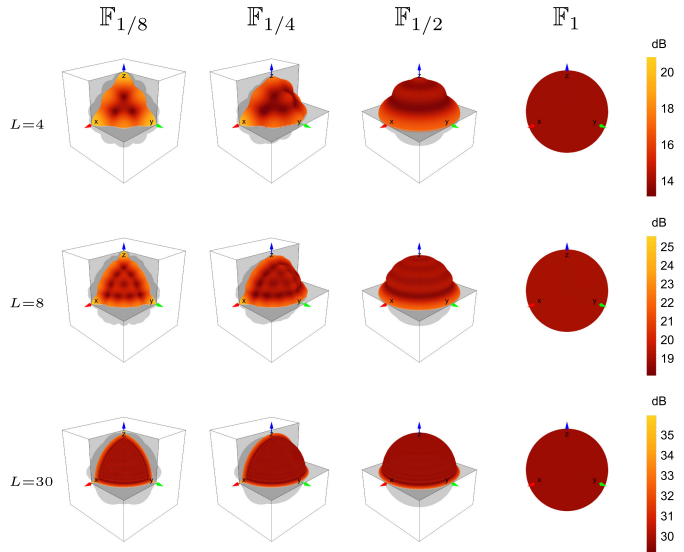


Fig. 8. Directivity Index of the beampattern $y_q(\theta, \phi)$ for all possible DOAs (θ_s, ϕ_s) in the solid angle of the SF \mathbb{F}_q , with $q \in \{1/8, 1/4, 1/2\}$ and for $L \in \{4, 8, 30\}$.

to be invariant by rotation. However, the DI is systematically better for grazing DOAs, at the boundary planes of the SFs. This value is even more important at the intersection of two boundary planes, for example for $(\theta_s = 90^\circ, \phi_s = 0^\circ)$. For these DOAs, all the image beampatterns add up and the DI increases consequently (see Fig. 5(a)).

a) Mean value: By averaging the DF_q of (38) for all possible DOAs in the solid angle offered by the SF \mathbb{F}_q , one obtains the mean value, denoted $\overline{\text{DF}}$ and given by:

$$\overline{\text{DF}}_q = \frac{1}{4\pi} \int_{\mathbb{F}_q} \text{DF}_q(\theta_s, \phi_s) \sin(\theta_s) d\phi_s d\theta_s, \quad (41)$$

where y_q is defined in (31). (41) can be further simplified by replacing DF in (38), then switching integral and sum, and finally using the orthonormality property of the SFHs. Thus, one shows

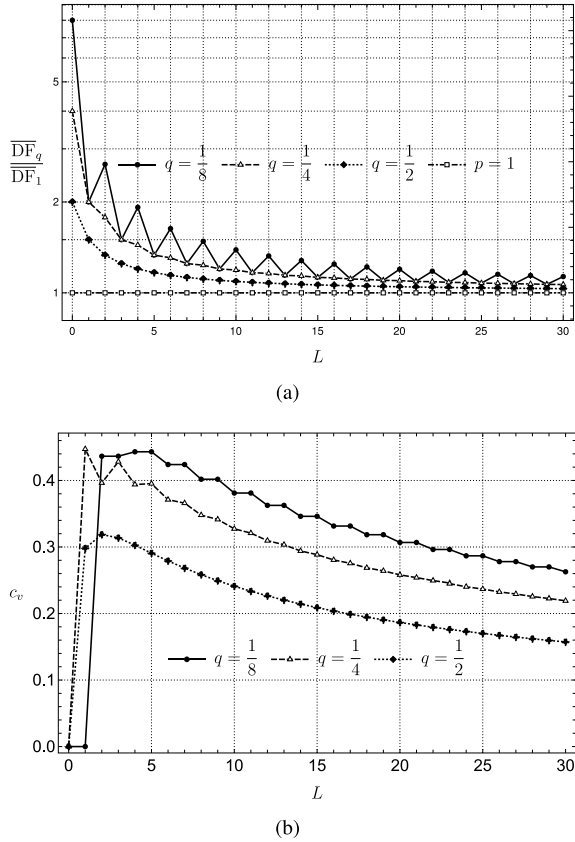


Fig. 9. (a) $\overline{DF}_q/\overline{DF}_1$: ratio of averages \overline{DF}_q and \overline{DF}_1 versus maximum degree L . (b) Coefficient of variation versus maximum degree L .

that:

$$\overline{DF}_q = \frac{1}{q} \sum_{l=0}^{\infty} \sum_{\substack{m=-l \\ (l,m) \in \mathbb{M}_q}}^l 1. \quad (42)$$

Therefore, for a maximum degree L , the average directivity factor is the number of SFHs of (23) divided by the SF value q :

$$\overline{DF}_q(L) = \frac{Q_q(L)}{q}. \quad (43)$$

To compare the average \overline{DF}_q of the bounded domains with the average of the unbounded one, the ratio $\overline{DF}_q/\overline{DF}_1$ is plotted on Fig. 9(a). It converges to 1, which means that the averages \overline{DF}_q and \overline{DF}_1 of the bounded domains converge to the value of the unbounded domain. This phenomenon can also be observed on the color scale in Fig. 8 for $L = 30$. Thus, beam patterns constructed in SF $q \in \{1/8, 1/4, 1/2\}$ are less and less corrupted by the image beam pattern interferences, as they are becoming narrower when L increases. One reaches the DF performances of the free field domain, furthermore with less SFHs required, as shown in Fig 2(b). For instance, the relative error on average directivity factor (DF) falls below 10% from $L = 40$ for SF $_{1/8}$, $L = 19$ for SF $_{1/4}$ and $L = 9$ for SF $_{1/2}$ for a gain about 7.27, 3.63, 1.82 times less SFHs than SHs respectively.

b) *Coefficient of Variation*: Although the average of the DF function, \overline{DF}_q , converges to that of the sphere in free field, it remains to prove that the shape of the DF function converges to a constant value (i.e., spherical shape), as observed in Fig. 8.

The Coefficient of Variation (c_v) criterion is used for this purpose. This quantity characterizes the standard deviation of the function with respect to its mean. It is defined as:

$$c_v = \frac{\sigma_{DF_q}}{\overline{DF}_q}, \quad (44)$$

where the standard deviation σ_{DF_q} is given by:

$$\sigma_{DF_q} = \sqrt{\frac{1}{q4\pi} \int_{\mathbb{F}_q} (DF_q(\theta_s, \phi_s) - \overline{DF}_q)^2 \sin(\theta_s) d\theta_s d\phi_s}.$$

In fact, the standard deviation σ_{DF_q} increases as L increases. This is due, on the one hand, to the fact that values far from the SF \mathbb{F}_q boundaries approach the mean value and contribute little to the standard deviation, and, on the other hand, to the fact that values close to these boundaries increase sharply, as shown in Fig. 8. Furthermore, the mean value \overline{DF}_q also increases with L . As shown in Fig. 9(b), the coefficient of variation decreases as L increases. This means that the function $DF_q(\theta_s, \phi_s)$ converges to a constant, i.e., to the value of the free field \overline{DF}_1 . Finally, as L increases, the SF \mathbb{F}_q regular beamformer converges to a rotationally-invariant one.

V. BEAMFORMING EXAMPLE

This section provides an example of beamforming for the different SFs \mathbb{F}_q . The acoustic scene consists of two unit amplitude plane waves P_1 and P_2 with DOAs $(\theta_1 = 75^\circ, \phi_1 = 15^\circ)$ and $(\theta_2 = 35^\circ, \phi_2 = 75^\circ)$ respectively. This gives an angle $\Theta \simeq 60.72^\circ$, from (33). Note that modal beamforming is applied here directly to the SFHs components of the sound field, using (27) and is independent of frequency. In practice, a SFMA can be used to obtain these components as the SMA is used to estimate the SHs components for the whole sphere [4]. However, the microphone number and positions bring spatial aliasing which gives an upper frequency limit for accurate estimation [22], [23]. As well, the array radius imposes a lower frequency limit for the accurate estimation of high degree components, due to limited dynamics for real-world applications when inverting the radial function in (25) [3]. Some SFMA examples are already available in the literature for the hemisphere [6], [7].

Using (27) the SFHs components of this acoustic scene are:

$$b_{l,m,p} = \frac{Y_{l,m,q}(\theta_1, \phi_1)}{\sum_{l=0}^L \sum_{\substack{m=-l \\ (l,m) \in \mathbb{M}_q}}^l Y_{l,m,q}(\theta_1, \phi_1)^2} + \frac{Y_{l,m,q}(\theta_2, \phi_2)}{\sum_{l=0}^L \sum_{\substack{m=-l \\ (l,m) \in \mathbb{M}_q}}^l Y_{l,m,q}(\theta_2, \phi_2)^2}, \quad (45)$$

where the denominators ensure unit-amplitude plane waves. Using (31) the beamformer output is computed for all steering angles $(\theta, \phi) \in (0, 90^\circ) \times (0, 90^\circ)$. The resulting magnitude $|\tilde{y}_q(\theta, \phi)|$ is plotted in Fig. 10 for $L \in \{4, 8, 30\}$. The two plane

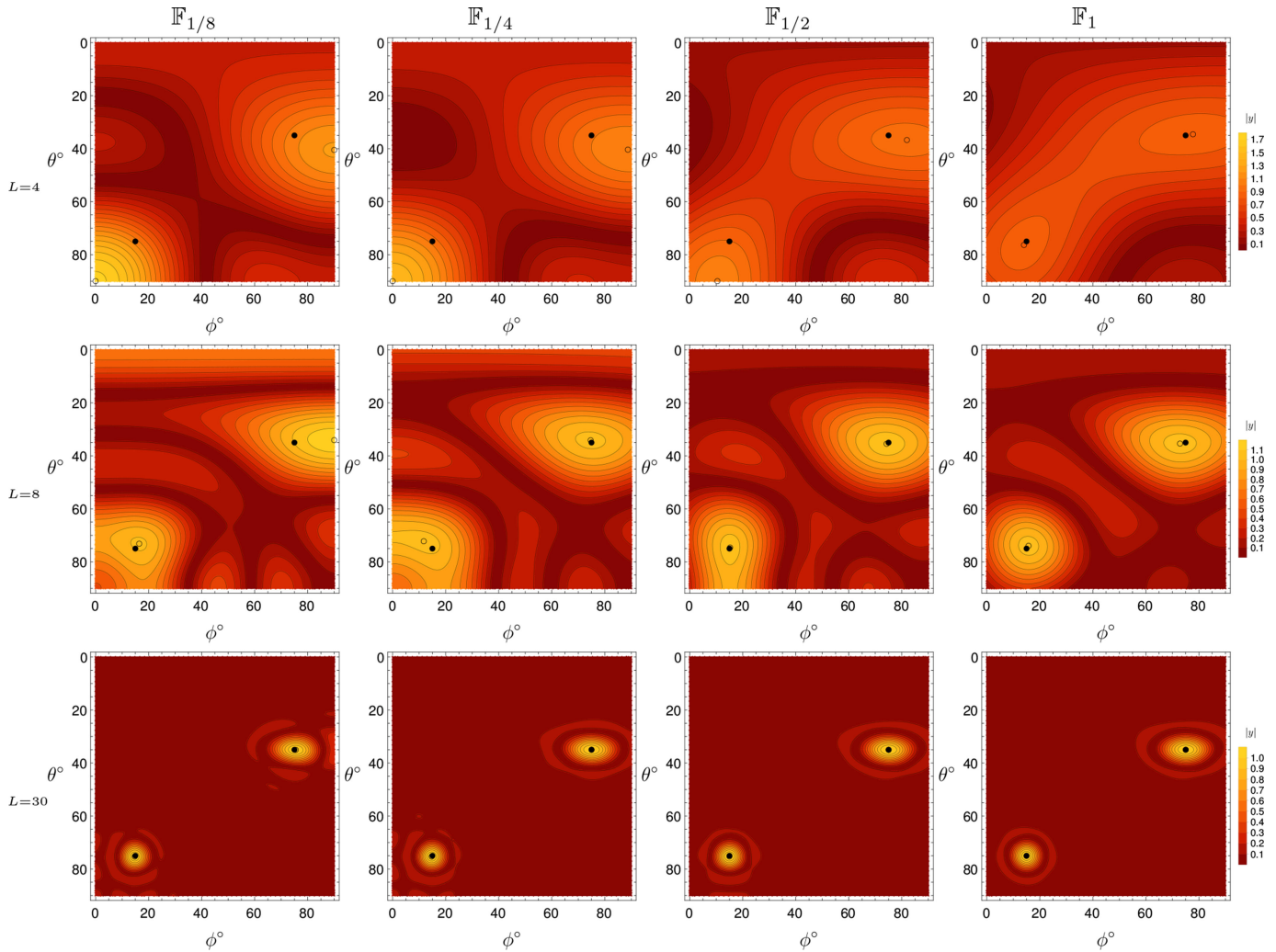


Fig. 10. Beamforming example: two unit-amplitude plane waves P_1 and P_2 , with DOAs $(\theta_1 = 75^\circ, \phi_1 = 15^\circ)$ and $(\theta_2 = 35^\circ, \phi_2 = 75^\circ)$ respectively, compose the acoustic scene. A regular beamformer is designed in the SFs \mathbb{F}_q with $q \in \{1/8, 1/4, 1/2\}$ and for $L \in \{4, 8, 30\}$. It is steered in directions $(\theta, \phi) \in (0^\circ, 90^\circ) \times (0^\circ, 90^\circ)$.

waves DOAs are marked with black dots. The two local maxima of $|\tilde{y}_q(\theta, \phi)|$ in the vicinity of P_1 and P_2 DOAs are marked with circles.

From Fig. 10, it can be observed that the more L increases, the closer the map maxima are located to the plane waves P_1 and P_2 DOAs and with the correct amplitudes. In the same way, the less the SF is bounded, the more accurate the location is.

For the free field, the scene contains two plane waves. As $\Theta \gg \Theta_{\text{lim}}$ in this example, the side lobes of the two beampatterns influence the position of the maxima on the map. However, for the SFs \mathbb{F}_q with $q \in \{1/8, 1/4, 1/2\}$, the image beampatterns of the two plane waves add up and degrade the localization result. For $L = 4$, plane wave P_1 and the SFs $\mathbb{F}_{1/8}, \mathbb{F}_{1/4}$ and $\mathbb{F}_{1/2}$, the angle between the wave P_1 and its images is such that $\Theta < \Theta_{\text{lim}}$. Thus, the maximum is found at $(0^\circ, 90^\circ)$, as explained in Section IV-B. As L increases and Θ_{lim} decreases (Fig. 6), the maxima are found closer to their correct location. For the order $L = 30$, the results are nearly identical for all domains. Tab III lists some values of interest for this analysis, in particular, the

number $Q_q(L)$ of SFHs involved to calculate the maps, the ratio with the SHs number to measure the gain in terms of functions to manipulate, the angular errors between the DOAs of P_1 and P_2 and the local maxima, denoted $\Psi_p(\theta_1, \phi_1)$ and $\Psi_p(\theta_2, \phi_2)$ respectively, as well as the beamformer amplitudes in the P_1 and P_2 DOAs. From Table III, the results converge rather quickly to the free field behaviour, but with less SFHs than SHs. Regarding the amplitudes in the plane waves DOAs, they can sometimes be closer to unity for the bounded domains than in the free field case. Again, this is the result of interferences between plane waves and their images. Note that the values of Table III depend on the acoustic scene, hence the interest of having average performance criteria as presented in the Secs. IV-B and IV-C.

VI. CONCLUSION

In this paper the beamforming on 1/8, 1/4, 1/2 spaces bounded with Neumann conditions has been studied. Using the SFHs decomposition approach, it has been shown that the number

TABLE III

SEVERAL INDICATORS FOR THE BEAMFORMING EXAMPLE OF FIG. 10: FOR EACH MAXIMAL DEGREE $L \in \{4, 8, 30\}$ AND EACH SF \mathbb{F}_q WITH $q \in \{1/8, 1/4, 1/2\}$ THE NUMBER OF SFHS Q_q IS GIVEN IN THE FIRST ROW, THE RATIO WITH THE NUMBER OF SHS IN SECOND ROW, THE BEAMFORMER OUTPUT $\tilde{y}_q(\theta_1, \phi_1)$ IN THE THIRD ROW, THE BEAMFORMER OUTPUT $\tilde{y}_q(\theta_2, \phi_2)$ IN THE FOURTH ROW, THE ANGULAR DISTANCE $\Psi_q(\theta_1, \phi_1)$ BETWEEN LOCAL MAXIMA AND (θ_1, ϕ_1) AND THE ANGULAR DISTANCE $\Psi_q(\theta_2, \phi_2)$ BETWEEN LOCAL MAXIMA AND (θ_2, ϕ_2)

	L	$\mathbb{F}_{1/8}$	$\mathbb{F}_{1/4}$	$\mathbb{F}_{1/2}$	\mathbb{F}_1
$Q_q(L)$	4	6	9	15	25
	8	15	25	45	81
	30	136	256	496	961
$Q_1(L)/Q_q(L)$	4	4.17	2.78	1.67	1
	8	5.4	3.24	1.8	1
	30	7.07	3.75	1.94	1
$\tilde{y}_q(\theta_1, \phi_1)$	4	1.05	0.96	0.90	0.85
	8	1.00	1.02	1.05	1.04
	30	1.00	1.00	1.01	1.01
$\tilde{y}_q(\theta_2, \phi_2)$	4	1.05	0.979	0.927	0.849
	8	1.00	1.03	1.05	1.04
	30	0.998	1.00	1.01	1.01
$\Psi_q(\theta_1, \phi_1)$	4	21.1°	21.1°	15.7°	1.64°
	8	2.31°	4.18°	0.455°	1.28°
	30	0.366°	0.399°	0.236°	0.0540°
$\Psi_q(\theta_2, \phi_2)$	4	10.7°	9.93°	4.41°	1.64°
	8	8.54°	0.898°	0.628°	1.28°
	30	0.288°	0.0268°	0.0417°	0.0549°

of functions to be used to realize a regular beamformer is smaller than the number of SHs used for the unbounded domain. However, the presence of rigid boundaries introduces image beampatterns that break the axi-symmetry and rotational invariance properties of regular beamformers of the unbounded case. The performance has been evaluated for the angular error on the maximum and the DF in the case of the response to a unit-amplitude plane wave. It has been shown that the angular resolution given for a maximal decomposition degree L determines the superposition of the image beampatterns and the beamformer performance. However, the latter improves and converges to the performance of the beamformer in the unbounded domain as L increases and as the SF is large. A case study to show the different phenomena involved in the analysis by beamforming of an acoustic field composed of two unit-amplitude plane waves is proposed.

Future work will seek to design beampattern weights optimized to mitigate the effect of image beampatterns. In addition, the robustness of beamforming with SFHs basis found for Neumann boundary conditions has to be studied in more realistic situations, such as in a room where the walls do not meet such boundary condition. The kind of processing proposed here makes it possible to use SFMA that are particularly suitable for integration in business premises or private homes; room corners are particularly common in many buildings. Thus, there are a wide range of applications, ranging from medical supervision of the elderly, to intrusion detection, voice commands, etc., which can be integrated into a building. The next step will therefore be

to develop and test the proposed geometries in order to evaluate their in situ performance.

APPENDIX A

CONDITIONS ON SHS INDICES (l, m) FOR SYMMETRY PLANES
 $x = 0, y = 0, z = 0$

In this appendix, the conditions on (l, m) indices such that the corresponding SHs present the symmetry planes $x = 0, y = 0$ or $z = 0$ are derived. This is done by replacing ϕ and θ in (13) and (16) into (18) for the even symmetries, and (14) and (17) into (18) for the odd symmetries. The writing uses Boolean algebra. In the following demonstrations, the multiplication properties of two even and/or odd numbers are used. The results are summarized in Table I.

A. Even Symmetry Plane $x = 0$

$$n \in \mathbb{Z} \wedge \left(m \in \mathbb{N}^* \wedge \left(\frac{\pi}{2} = \frac{2n\pi}{m} \vee \frac{3\pi}{2} = \frac{2n\pi}{m} \right) \right)$$

$$\vee m \in \mathbb{Z}^- \wedge \left(\frac{\pi}{2} = \frac{2n\pi}{m} + \frac{\pi}{2m} \vee \frac{3\pi}{2} = \frac{2n\pi}{m} + \frac{\pi}{2m} \right)$$

$$\vee 0 = \frac{\pi}{2} \vee \pi = \frac{\pi}{2}$$

$$\iff n \in \mathbb{Z} \wedge (m \in \mathbb{N}^* \wedge (m = 4n \vee 3m = 4n))$$

$$\vee m \in \mathbb{Z}^- \wedge (m = 4n + 1 \vee 3m = 4n + 1))$$

$$\iff m \in 2\mathbb{N} \vee m \in 2\mathbb{Z}^- + 1. \quad (46)$$

B. Odd Symmetry Plane $x = 0$

$$n \in \mathbb{Z} \wedge \left(m \in \mathbb{Z}^- \wedge \left(\frac{\pi}{2} = \frac{2n\pi}{m} \vee \frac{3\pi}{2} = \frac{2n\pi}{m} \right) \right)$$

$$\vee m \in \mathbb{N}^* \wedge \left(\frac{\pi}{2} = \frac{2n\pi}{m} + \frac{\pi}{2m} \vee \frac{3\pi}{2} = \frac{2n\pi}{m} + \frac{\pi}{2m} \right)$$

$$\vee 0 = \frac{\pi}{2} \vee \pi = \frac{\pi}{2}$$

$$\iff n \in \mathbb{Z} \wedge (m \in \mathbb{Z}^- \wedge (m = 4n \vee 3m = 4n))$$

$$\vee m \in \mathbb{N}^* \wedge (m = 4n + 1 \vee 3m = 4n + 1))$$

$$\iff m \in 2\mathbb{N} + 1 \vee m \in 2\mathbb{Z}^-. \quad (47)$$

C. Even Symmetry Plane $y = 0$

$$n \in \mathbb{Z} \wedge \left(m \in \mathbb{N}^* \wedge \left(\pi = \frac{2n\pi}{m} \vee 2\pi = \frac{2n\pi}{m} \right) \right)$$

$$\vee m \in \mathbb{Z}^- \wedge \left(\pi = \frac{2n\pi}{m} + \frac{\pi}{2m} \vee 2\pi = \frac{2n\pi}{m} + \frac{\pi}{2m} \right)$$

$$\vee 0 = \frac{\pi}{2} \vee \pi = \frac{\pi}{2}$$

$$\iff n \in \mathbb{Z} \wedge (m \in \mathbb{N} \wedge (m = 2n \vee m = n))$$

$$\begin{aligned} & \forall m \in \mathbb{Z}^- \wedge (2m = 4n + 1 \vee 4m = 4n + 1) \\ \iff & m \in \mathbb{N}. \end{aligned} \quad (48)$$

D. Odd Symmetry Plane $y = 0$

$$\begin{aligned} & n \in \mathbb{Z} \wedge \left(m \in \mathbb{Z}^- \wedge \left(\pi = \frac{2n\pi}{m} \vee 2\pi = \frac{2n\pi}{m} \right) \right. \\ & \forall m \in \mathbb{N}^* \wedge \left(\pi = \frac{2n\pi}{m} + \frac{\pi}{2m} \vee 2\pi = \frac{2n\pi}{m} + \frac{\pi}{2m} \right) \\ & \forall 0 = \frac{\pi}{2} \vee \pi = \frac{\pi}{2} \\ \iff & n \in \mathbb{Z} \wedge \left(m \in \mathbb{Z}^- \wedge (m = 2n \vee m = n) \right. \\ & \left. \forall m \in \mathbb{N}^* \wedge (2m = 4n + 1 \vee 4m = 4n + 1) \right) \\ \iff & m \in \mathbb{Z}^-. \end{aligned} \quad (49)$$

E. Even Symmetry Plane $z = 0$

$$\begin{aligned} & \frac{\pi}{2} = \frac{\pi}{2} \wedge (l + m) \in 2\mathbb{Z} \\ \iff & (l + m) \in 2\mathbb{Z}. \end{aligned} \quad (50)$$

F. Odd Symmetry Plane $z = 0$

$$\begin{aligned} & \frac{\pi}{2} = \frac{\pi}{2} \wedge (l + m) \in 2\mathbb{Z} + 1 \\ \iff & (l + m) \in 2\mathbb{Z} + 1. \end{aligned} \quad (51)$$

APPENDIX B SETS \mathbb{M}_q DERIVATION

In this Appendix, the sets \mathbb{M}_q of Section III-C are derived with the following method: for each SF domain \mathbb{F}_q , by using 3, the domain boundaries planes are identified. Then, the conditions on (l, m) indices for the corresponding planes in Table I are used to build the set.

A. $\mathbb{M}_{1/8}$

From 3, the $Y_{l,m,1/8}$ family is made of SHs having the following conditions for their symmetry planes:

$$\{x = 0\} \wedge \{y = 0\} \wedge \{z = 0\}. \quad (52)$$

Then, by using the relationships in Table I the set $\mathbb{M}_{1/8}$ is build:

$$\begin{aligned} \mathbb{M}_{1/8} &= \{(l, m) \in (\mathbb{N}, \mathbb{Z}) \mid |m| \leq l \wedge (m \in 2\mathbb{N} \vee m \in 2\mathbb{Z}^- + 1) \\ & \quad \wedge m \in \mathbb{N} \wedge (l + m) \in 2\mathbb{Z}\} \\ &= \{(l, m) \in (\mathbb{N}, \mathbb{Z}) \mid m \leq l \wedge m \in 2\mathbb{N} \wedge (l + m) \in 2\mathbb{N}\} \\ &= \{(l, m) \in (\mathbb{N}, \mathbb{Z}) \mid m \leq l \wedge l \in 2\mathbb{N} \wedge m \in 2\mathbb{N}\}. \end{aligned} \quad (53)$$

B. $\mathbb{M}_{1/4}$

From 3, the $Y_{l,m,1/4}$ family is made of SHs having the following conditions for their symmetry planes:

$$\{y = 0\} \wedge \{z = 0\}. \quad (54)$$

Then, by using the relationships in Table I the set $\mathbb{M}_{1/4}$ is build:

$$\begin{aligned} \mathbb{M}_{1/4} &= \{(l, m) \in (\mathbb{N}, \mathbb{Z}) \mid |m| \leq l \wedge m \in \mathbb{N} \wedge (l + m) \in 2\mathbb{Z}\} \\ &= \{(l, m) \in (\mathbb{N}, \mathbb{Z}) \mid m \leq l \wedge m \in \mathbb{N} \wedge (l + m) \in 2\mathbb{N}\}. \end{aligned} \quad (55)$$

C. $\mathbb{M}_{1/2}$

From 3, the $Y_{l,m,1/2}$ family is made of SHs having the following conditions for their symmetry planes:

$$\{z = 0\}. \quad (56)$$

Then, by using the relationships in Table I the set \mathbb{M}_3 is build:

$$\mathbb{M}_3 = \{(l, m) \in (\mathbb{N}, \mathbb{Z}) \mid |m| \leq l \wedge (l + m) \in 2\mathbb{Z}\}. \quad (57)$$

APPENDIX C SFHS ORTHONORMALITY

In this Appendix, the SFHS orthonormality property is detailed (see Section III-D). The inner product of (4) and the symmetry properties of the SFHS $Y_{l,m,q}$ are used in the demonstration. The demonstration is done for the family $Y_{l,m,1/8}$.

From (4) for two SFHS $Y_{l,m,1/8}$ and $Y_{l',m',1/8}$, one has:

$$\begin{aligned} & \langle Y_{l,m,1/8}, Y_{l',m',1/8} \rangle \\ &= \int_{\mathbb{F}_{1/8}} Y_{l,m,1/8}(\theta, \phi) Y_{l',m',1/8}(\theta, \phi) \sin(\theta) d\theta d\phi. \end{aligned} \quad (58)$$

Using (1) with (3), one has:

$$\begin{aligned} & \langle Y_{l,m,1/8}, Y_{l',m',1/8} \rangle \\ &= \int_{\phi=0}^{\pi/2} \int_{\theta=0}^{\pi/2} Y_{l,m,1/8}(\theta, \phi) Y_{l',m',1/8}(\theta, \phi) \sin(\theta) d\theta d\phi. \end{aligned} \quad (59)$$

By exploiting the SFHS Y_{l,m,\mathbb{F}_1} symmetry with respect to ϕ and θ variables, the latter equation becomes:

$$\begin{aligned} & \langle Y_{l,m,\mathbb{F}_2}, Y_{l',m',\mathbb{F}_2} \rangle \\ &= \frac{1}{8} \int_{\phi=0}^{2\pi} \int_{\theta=0}^{\pi} Y_{l,m,1/8}(\theta, \phi) Y_{l',m',1/8}(\theta, \phi) \sin(\theta) d\theta d\phi. \end{aligned} \quad (60)$$

The SFHS $Y_{l,m,1/8}$ are orthogonal on $\mathbb{L}^2(\mathbb{F}_1)$, therefore, using (19) one obtains:

$$\langle Y_{l,m,1/8}, Y_{l',m',1/8} \rangle = \frac{1}{8} N_{1/8}^2 \delta_{l,l'} \delta_{m,m'}. \quad (61)$$

Consequently, the SFHS $Y_{l,m,1/8}$ are orthogonal on $\mathbb{F}_{1/8}$ and to ensure orthonormality one has:

$$N_{1/8} = 2\sqrt{2}. \quad (62)$$

Following the same reasoning, one shows the orthonormality for all SFHs $Y_{l,m,q}$ with $q \in \{1/4, 1/2\}$. The norm values N_q are summarized in the right column of Table II.

APPENDIX D SFHS NUMBER $Q_q(L)$

In this Appendix, the SFHs number up to a degree L are derived as closed form formulas. The results are summarized in Table II. In the following computations, $\lfloor \cdot \rfloor$ are $\lceil \cdot \rceil$ floor and ceiling functions respectively.

A. $Q_{1/8}(L)$

$$\begin{aligned} Q_{1/8}(L) &= \sum_{\substack{l=0 \\ l \in 2\mathbb{N}}}^L \sum_{\substack{m=0 \\ m \in 2\mathbb{N}}}^l 1 \\ &= \sum_{\substack{l=0 \\ l \in 2\mathbb{N}}}^L \left(\frac{l}{2} + 1 \right) = (\lfloor L/2 \rfloor + 1) + \sum_{\substack{l=0 \\ l \in 2\mathbb{N}}}^L l/2 \\ &= (\lfloor L/2 \rfloor + 1) + \sum_{l=0}^{\lfloor L/2 \rfloor} l \\ &= \frac{1}{2} (\lfloor L/2 \rfloor + 1) (\lfloor L/2 \rfloor + 2). \end{aligned} \quad (63)$$

B. $Q_{1/4}(L)$

$$\begin{aligned} Q_{1/4}(L) &= \sum_{\substack{l=0 \\ (l+m) \in 2\mathbb{N}}}^L \sum_{\substack{m=0 \\ m \in 2\mathbb{N}}}^l 1 = \sum_{\substack{l=0 \\ l \in 2\mathbb{N}}}^L \sum_{\substack{m=0 \\ m \in 2\mathbb{N}}}^l 1 + \sum_{\substack{l=1 \\ l \in 2\mathbb{N}+1}}^L \sum_{\substack{m=1 \\ m \in 2\mathbb{N}+1}}^l 1 \\ &= Q_{1/8}(L) + \sum_{\substack{l=1 \\ l \in 2\mathbb{N}+1}}^L \sum_{\substack{m=1 \\ m \in 2\mathbb{N}+1}}^l 1 \\ &= \frac{1}{2} (\lfloor L/2 \rfloor + 1) (\lfloor L/2 \rfloor + 2) + \sum_{\substack{l=1 \\ l \in 2\mathbb{N}+1}}^L \lfloor l/2 \rfloor \\ &= \frac{1}{2} (\lfloor L/2 \rfloor + 1) (\lfloor L/2 \rfloor + 2) + \frac{1}{2} \lfloor L/2 \rfloor (\lfloor L/2 \rfloor + 1) \\ &= \frac{1}{2} ((\lfloor L/2 \rfloor + 1) (\lfloor L/2 \rfloor + 2) \\ &\quad + ((L-1)/2 + 1) ((L-1)/2 + 2)). \end{aligned} \quad (64)$$

C. $Q_{1/2}(L)$

$$\begin{aligned} Q_{1/2}(L) &= \sum_{\substack{l=0 \\ (l+m) \in 2\mathbb{N}}}^L \sum_{\substack{m=-l \\ m \in 2\mathbb{N}}}^l 1 \\ &= \sum_{\substack{l=0 \\ l \in 2\mathbb{N}}}^L \sum_{\substack{m=-l \\ m \in 2\mathbb{N}}}^l 1 + \sum_{\substack{l=1 \\ l \in 2\mathbb{N}+1}}^L \sum_{\substack{m=-l \\ m \in 2\mathbb{N}+1}}^l 1 \end{aligned}$$

$$\begin{aligned} &= \sum_{\substack{l=0 \\ l \in 2\mathbb{N}}}^L (l+1) + \sum_{\substack{l=1 \\ l \in 2\mathbb{N}+1}}^L (l+1) \\ &= \sum_{l=0}^L (l+1) = 1/2(L+1)(L+2). \end{aligned} \quad (65)$$

D. $Q_1(L)$

$$Q_1(L) = \sum_{l=0}^L \sum_{m=-l}^l 1 = \sum_{l=0}^L (2l+1) = (L+1)^2 \quad (66)$$

APPENDIX E PLANE WAVE REPRESENTATION IN THE NEUMANN-BOUNDED OCTANT UNION DOMAIN \mathbb{O}_3

In this Appendix, (26) is proven in the case of a rigid bounded domain \mathbb{O}_3 , that is to say a rigid bounded half-space. The angular part of the solution is described in $\mathbb{L}_{1/2}$ using SFHs $Y_{l,m,\mathbb{F}_{1/2}}$.

Let us consider a plane wave with direction of arrival (θ_s, ϕ_s) in $\mathbb{O}_{1/2}$. A rigid plane is placed at \mathbb{O}_3 boundary, that is to say such that $\theta = \frac{\pi}{2}$ (or $z = 0$). According to the image source principle [20] the acoustic pressure is due to a plane wave coming from (θ_s, ϕ_s) and a plane wave coming from $(\pi - \theta, \phi_s)$. Using (26) in the free space one has:

$$\begin{aligned} p(k, r, \theta, \phi) &= \sum_{l=0}^L \sum_{\substack{m=-l \\ (l,m) \in \mathbb{M}_{1/2}}}^l i^l j_l(kr) \\ &\quad (Y_{l,m}(\theta_s, \phi_s) + Y_{l,m}(\pi - \theta_s, \phi_s)) Y_{l,m}(\theta, \phi). \end{aligned} \quad (67)$$

Then, one splits the sums for $(l, m) \in \mathbb{M}_{1/2}$ and $(l, m) \notin \mathbb{M}_{1/2}$:

$$\begin{aligned} p(k, r, \theta, \phi) &= \sum_{\substack{l=0 \\ (l,m) \in \mathbb{M}_{1/2}}}^L \sum_{\substack{m=-l \\ m \in \mathbb{M}_{1/2}}}^l i^l j_l(kr) (Y_{l,m}(\theta_s, \phi_s) \\ &\quad + Y_{l,m}(\pi - \theta_s, \phi_s)) Y_{l,m}(\theta, \phi) \\ &\quad + \sum_{\substack{l=0 \\ (l,m) \notin \mathbb{M}_{1/2}}}^L \sum_{\substack{m=-l \\ m \in \mathbb{M}_{1/2}}}^l i^l j_l(kr) (Y_{l,m}(\theta_s, \phi_s) \\ &\quad + Y_{l,m}(\pi - \theta_s, \phi_s)) Y_{l,m}(\theta, \phi). \end{aligned} \quad (68)$$

As shown in Section II-E, for $(l, m) \in \mathbb{M}_{1/2}$, the plane of symmetry $\theta = \frac{\pi}{2}$ is an even symmetry plane. As well, for $(l, m) \notin \mathbb{M}_{1/2}$, $\theta = \frac{\pi}{2}$ is an odd symmetry plane. As a consequence one has:

$$\begin{cases} Y_{l,m}(\theta, \phi) = Y_{l,m}(\pi - \theta, \phi) & \text{for } (l, m) \in \mathbb{M}_{1/2} \\ Y_{l,m}(\theta, \phi) = -Y_{l,m}(\pi - \theta, \phi) & \text{for } (l, m) \notin \mathbb{M}_{1/2}. \end{cases} \quad (69)$$

Using (69) into (68) one obtains:

$$p(k, r, \theta, \phi) = 2 \sum_{l=0}^L \sum_{\substack{m=-l \\ (l,m) \in \mathbb{M}_{1/2}}}^l i^l j_l(kr) Y_{l,m}(\theta_s, \phi_s) Y_{l,m}(\theta, \phi). \quad (70)$$

Finally, using (19) with Tab. (II) one has:

$$p(k, r, \theta, \phi) = \sum_{l=0}^L \sum_{\substack{m=-l \\ (l,m) \in \mathbb{M}_{1/2}}}^l i^l j_l(kr) Y_{l,m,1/2}(\theta_s, \phi_s) Y_{l,m,1/2}(\theta, \phi). \quad (71)$$

The demonstration for other domains \mathbb{O}_q is similar.

REFERENCES

- [1] V. Pulkki, S. Delikaris-Manias, and A. Politis, *Parametric Time-Frequency Domain Spatial Audio*. Hoboken, NJ, USA: John Wiley & Sons, 2017.
- [2] F. Zotter and M. Frank, "Ambisonics - A Practical 3D Audio Theory for Recording, Studio Prod., Sound Reinforcement, and Virtual Reality," ser. Springer Topics in Signal Processing, Cham, Switzerland: Springer, 2019.
- [3] B. Rafaely, *Fundamentals Spherical Array Process.*, 2nd ed., Cham, Switzerland: Springer, 2019.
- [4] J. Meyer and G. Elko, "A highly scalable spherical microphone array based on an orthonormal decomposition of the soundfield," in *Proc. IEEE Int. Conf. Acoust. Speech, Signal Process.*, 2002, vol. 2, pp. 1781–1784.
- [5] M. Brandstein and D. Ward, *Microphone Arrays: Signal Process. Techn. Appl.* Berlin, Germany: Springer, 2001.
- [6] Z. Li and R. Duraiswami, "Hemispherical microphone arrays for sound capture and beamforming," in *Proc. IEEE Workshop Appl. Signal Process. Audio Acoust.*, 2005, pp. 106–109.
- [7] M. Melon, C. Langrenne, P. Herzog, and A. Garcia, "Evaluation of a method for the measurement of subwoofers in usual rooms," *J. Acoust. Soc. Amer.*, vol. 127, no. 1, pp. 256–263, Jan. 2010.
- [8] H. Pomberger and F. Pausch, "Design and evaluation of a spherical segment array with double cone," *Acta Acustica United Acustica*, vol. 100, no. 5, pp. 921–927, 2014.
- [9] B.-D. Keller and F. Zotter, "A New Prototype for Sound Projection," in *Fortschritte Der Akustik - DAGA*. Nürnberg, Germany: DEGA, 2015.
- [10] H. Pomberger, "Acoustic boundary value problems and their application to partial spherical microphone arrays," Ph.D. dissertation, Univ. of Music and Performing Arts, Graz, Austria, 2017.
- [11] F. J. Simons and F. A. Dahlen, "Spherical Slepian functions and the polar gap in geodesy," *Geophysical J. Int.*, vol. 166, no. 3, pp. 1039–1061, 2006.
- [12] F. Zotter and H. Pomberger, "Spherical slepian functions for approximation of spherical measurement data," in *Fortschritte Der Akustik - DAGA*. Darmstadt, Germany: DEGA, 2012.
- [13] H. Pomberger and F. Zotter, "Modal Sound Field Decomposition Applicable for a Limited Range of Directions," in *Fortschritte Der Akustik - AIA-DAGA*. Merano, Germany: DEGA, 2013.
- [14] B. Rafaely, "Plane-wave decomposition of the sound field on a sphere by spherical convolution," *J. Acoust. Soc. Amer.*, vol. 116, no. 4, pp. 2149–2157, 2004.
- [15] E. G. Williams, *Fourier Acoust.: Sound Radiation And Nearfield Acoustical Holography*. London, U.K.: Academic Press, 1999.
- [16] G. B. Arfken and H. J. Weber, *Math. Methods for Physicists*, 6th ed. Elsevier, 2005.
- [17] M. Chapman, "Symmetries of Spherical Harmonics: Applications to ambisonics," in *Proc. Ambisonics Symp.* Graz: IEM, 2009, pp. 1–14.
- [18] M. A. Al-Gwaiz, *Sturm-Liouville Theory and Its Appl.* London, UK: Springer, 2008.

- [19] M. Bruneau, *Fundamentals of acoustics*. London, UK: ISTE, 2006.
- [20] J. B. Allen and D. A. Berkley, "Image method for efficiently simulating small-room acoustics," *J. Acoust. Soc. Amer.*, vol. 65, no. 4, pp. 943–950, 1979.
- [21] A. H. Nuttall and B. A. Cray, "Approximations to directivity for linear, planar, and volumetric apertures and arrays," *IEEE J. Ocean. Eng.*, vol. 26, no. 3, pp. 383–398, Jul. 2001.
- [22] B. Rafaely, B. Weiss, and E. Bachmat, "Spatial aliasing in spherical microphone arrays," *IEEE Trans. Signal Process.*, vol. 55, no. 3, pp. 1003–1010, Mar. 2007.
- [23] P. Lecomte, P.-A. Gauthier, C. Langrenne, A. Berry, and A. Garcia, "A fifty-node Lebedev grid and its applications to ambisonics," *J. Audio Eng. Soc.*, vol. 64, no. 11, pp. 868–881, 2016.



Pierre Lecomte was born in France, in 1989. He received the Dipl.Ing. degree from Arts et Métiers Engineer School, Metz, France, in 2012, the M.Sc. degree from Centrale Paris Engineer School, Paris, France, in 2012, the M.Sc. degree from University Paris VI, Paris, France, in 2013, and the Ph.D. degree in mechanical engineering from the University of Sherbrooke, Sherbrooke, QC, Canada and Conservatoire National des Arts et Métiers, Paris, France, in 2016. He was a Postdoctoral Fellow with Lyon University, Lyon, France, from 2017 to 2018 and with Le Mans University, Le Mans, France, from 2018 to 2019. He is currently an Associate Professor with University Lyon 1, Lyon France. His research has been concerned with spatial audio, array signal processing and acousto-optics.



Manuel Melon was born in France, in 1969. He received the M.Sc. degree from Le Mans University, Le Mans, France, in 1992, and the Ph.D. degree on the ultrasonic characterization of damping materials, in 1996. Afterward, he joined the National Engineering Conservatory (Conservatoire National des Arts et Métiers) in Paris as an Associate Professor. In 2014, he was awarded a professorship with full tenure with the Acoustic Laboratory, Le Mans, where he co-supervises the International master's degree in electroacoustics (IMDEA). His research emphasis

lies in the fields of near-field acoustic holography, electroacoustics and signal processing. Prof. Melon was the treasurer of the French Acoustical Society from 2004 to 2007 and a long-time member of the SFA electroacoustical group (GTEA) board. He was inducted as a Fellow into the Audio Engineering Society in 2005.



Laurent Simon (Member, IEEE) was born in France, in 1965. He received the Ph.D. degree in acoustics from Le Mans University, Le Mans, France, in 1994. He is currently a Professor with the Acoustics Laboratory, Le Mans University (LAUM, UMR-CNRS 6613). His research interests mainly concern signal processing for acoustics and audio, including non-linear system identification, spectral estimation of missing data and array processing.